environments

Article

Hydrological Vulnerability Assessment of the Pañe Reservoir Using Spatially Distributed Modeling in Google Earth Engine Under CMIP6 Climate Scenarios and Increasing Water Demand

Flor de Liz Alvarez Cabana [1], Sebastian Adolfo Zuñiga Medina [2], Sonia Lazarte Arredondo [3], Rosa María Morán Silva [4], Jorge Polanco-Argüelles [5], Ronny Ivan Gonzales Medina [6] and Juan Adriel Carlos Mendoza [1,*]

1 Facultad de Ingeniería de Procesos, Universidad Nacional de San Agustín de Arequipa, Arequipa 04001, Peru; falvarez@unsa.edu.pe
2 Facultad de Geología, Geofísica y Minas, Universidad Nacional de San Agustín de Arequipa, Arequipa 04001, Peru; szunigam@unsa.edu.pe
3 Facultad de Arquitectura e Ingenierías Civil y del Ambiente, Escuela Profesional de Ingeniería Ambiental, Universidad Católica de Santa María, Arequipa 04001, Peru; slazarte@ucsm.edu.pe
4 Facultad de Ciencias, Universidad Nacional del Santa, Chimbote 02710, Peru; rmoran@uns.edu.pe
5 Facultad de Ingeniería Industrial y Mecánica, Universidad Tecnológica del Perú, Arequipa 04001, Peru; jpolanco@utp.edu.pe
6 Facultad de Ciencias Naturales y Formales, Universidad Nacional de San Agustín de Arequipa, Arequipa 04001, Peru; rgonzalesme@unsa.edu.pe
* Correspondence: jcarlosme@unsa.edu.pe; Tel.: +51-970-801-220

Abstract

Climate change and increasing water demand threaten water security in strategic high-Andean reservoirs by altering seasonal water availability, increasing evaporative losses, and intensifying pressure on regulated storage. This study assesses the hydrological vulnerability of the Pañe Reservoir, Arequipa, Peru, under CMIP6 scenarios SSP2-4.5 and SSP5-8.5 and three water-demand trajectories projected to 2100. A reservoir-scale water-balance model was calibrated using a genetic algorithm with CHIRPS precipitation and ERA5-Land temperature data, achieving satisfactory performance in calibration (NSE = 0.886; R^2 = 0.907) and validation (NSE = 0.888; R^2 = 0.891). Climate projections from MPI-ESM1-2-LR, EC-Earth3-Veg-LR, and EC-Earth3 were bias-corrected using Quantile Delta Mapping. Under baseline demand, active storage maintains positive trends of $+1.3 \times 10^6$ to $+2.2 \times 10^6$ m^3/decade; however, a 100% demand increase produces negative trends of up to -2.8×10^6 m^3/decade under SSP2-4.5. Effective precipitation increases by +0.123 and +0.283 mm/day under SSP2-4.5 and SSP5-8.5, respectively, while Rx5day and Rx10day rise by +5.43/+8.78 and +12.13/+19.42 mm/decade. These trends suggest greater wet-season concentration of water inputs, but not necessarily improved dry-season security under rising demand. Reservoir warming reaches +0.60 °C/decade under SSP5-8.5, which may increase evaporative losses and could create conditions more favorable to water-quality deterioration. Overall, future vulnerability in the Pañe system reflects the imbalance between increasing withdrawals and the reservoir's capacity to regulate highly seasonal high-Andean inflows, highlighting the need for demand control, loss reduction, bofedal protection and complementary wet-season storage.

Keywords: reservoir vulnerability; CMIP6 projections; Quantile Delta Mapping; high-Andean hydrology; water demand scenarios; critical storage days; Pañe

Check for updates

Academic Editors: Pengxiao Zhou, Qianqian Zhang, Fei Zhang and Zoe Li

Received: 19 May 2026
Revised: 26 June 2026
Accepted: 29 June 2026
Published: 14 July 2026

Copyright: © 2026 by the authors. Licensee MDPI, Basel, Switzerland. This article is an open access article distributed under the terms and conditions of the Creative Commons Attribution (CC BY) license.

1. Introduction

Freshwater is one of the most strategic resources for human development, but its availability faces growing pressures stemming from both climatic and anthropogenic factors [1,2]. Mountain regions and semi-arid areas, where water supply depends on seasonal precipitation and natural catchment regulation, are affected by climate change, which is progressively altering precipitation patterns and temperatures, impacting surface runoff and baseflow [3,4]. These changes disrupt the catchment water balance, and water storage becomes hydrologically vulnerable when altered climate forcing and increasing anthropogenic pressure erode the system's ability to perform its regulatory and supply functions [2,5]. The increase in demand driven by population growth, the expansion of irrigation, and economic development amplifies exposure and exacerbates vulnerability even under moderate scenarios [6,7]. Hydrological vulnerability is defined as the degree to which the reservoir system is susceptible to losing its capacity to store and regulate water under combined climatic and anthropogenic pressures. Operationally, this vulnerability is evaluated through changes in active storage, the frequency of critical-storage days, and the tendency of the reservoir to approach or fall below predefined operational thresholds under future climate and demand scenarios [2,5,6].

In this context, reservoirs are critical infrastructure for regulating water supply, supporting productive uses, and mitigating the effects of droughts; however, their performance is intrinsically linked to the variability and seasonality of inflows [8,9]. A recent study of the Haditha Dam quantified this dependency, showing that a projected 18% reduction in average flow under CMIP6 scenarios may translate into up to a 15% loss in hydroelectric production and significant storage depletion [10]. High-Andean basins present particularly challenging conditions, as they exhibit marked wet-dry seasonality, high climate sensitivity, complex topography, and a sparse observation network [11,12]. In Peru, Quiroz et al. [13] projects increases of up to 42% in inflows during the wet season in southern Peruvian catchments with negligible changes during the dry months, underscoring the acute problem of seasonality faced by operators.

In light of these challenges, the evolution of hydrological modeling over the past two decades reflects a shift from aggregate approaches toward spatially distributed frameworks capable of capturing the heterogeneity of terrain, land cover, and meteorological forcing at the grid cell level [12,14]. Concurrently, the integration of remote sensing data and gridded precipitation products such as CHIRPS, as well as surface temperature and soil hydrological properties from OpenLandMap, enables robust model parameterization in data-scarce environments [15,16]. In the field of climate projections, CMIP6 structures future scenarios using Shared Socioeconomic Pathways (SSP), which integrate emission pathways with different socioeconomic development contexts [3,4]. In addition, bias correction techniques such as Quantile Delta Mapping (QDM) are particularly relevant, as they correct systematic deviations from the observed time series and preserve the climate change signals in downscaled projections [3].

Despite these advances, a critical gap remains in the literature, as most studies analyze the impacts of climate change on reservoirs and the pressures associated with rising water demand in isolation [6,17,18]. Added to this is the prevalence of aggregate approaches that provide a limited representation of the spatial heterogeneity characteristic of high-mountain catchments, particularly in settings marked by a low density of hydrometeorological observations and by economic constraints that limit data generation [19,20]. Studies that simultaneously integrate semi-distributed hydrological modeling with CMIP6 projections under multiple SSP scenarios, and rising demand trajectories to assess the vulnerability of high-Andean reservoirs are notably scarce [21,22]. This gap is particularly relevant for the Pañe reservoir, where the interaction between shifts in rainfall patterns, growing demand

for irrigation and downstream urban water use creates a compound risk that aggregate frameworks fail to capture [23–25].

To address this gap, Google Earth Engine (GEE) offers a cloud-based platform capable of integrating spatial datasets from multiple sources and long-term climate time series, thereby facilitating the development of algorithms that can model the hydrological dynamics of a catchment with substantially greater computational efficiency than traditional desktop workflows [15,26]. Furthermore, GEE enables the processing of precipitation, temperature, land cover, and terrain data at the catchment scale in environments with limited in situ instrumentation [27,28]. On this basis, this study develops and applies a semi-distributed modeling framework implemented in GEE to assess the hydrological vulnerability of the Pañe reservoir under CMIP6 climate scenarios and projected increases in water demand, identifying changes in catchment inflows, storage dynamics, and reservoir operating conditions across the 21st century [12,13]. This approach provides a replicable methodology for data-scarce, high-altitude Andean reservoirs subject to complex hydroclimatic and socioeconomic pressures.

2. Materials and Methods

2.1. Study Area: The Pañe Reservoir Catchment

The Pañe Reservoir catchment is located in the northeastern part of the Arequipa region, within the district of Callalli, Caylloma province, near the administrative boundaries with Cusco and Puno regions (Figure 1) [29]. This catchment is part of the Colca-Majes-Camaná river basin, and its primary function is the regulation and provision of high-Andean interbasin water transfer for downstream urban and agricultural supply [30–32]. It extends between 15°17′42″ and 15°25′15″ S and approximately 71°04′ W longitude, covering an area of approximately 196.2 km^2 and ranging in elevation from 4584 to 5214 m a.s.l. These altitudinal and geographic conditions largely determine the climatic, hydrological, and ecological dynamics of the system [33–35]. The geology of the area is dominated by the Pañe-Luli-Yauri volcanic corridor, whose lithology—composed mainly of andesitic pyroclastics—favors high permeability due to fracturing and the development of volcanic and volcano-sedimentary aquifers that play an important role in recharge processes and in sustaining baseflow [36–38]. Peatlands with high soil moisture content develop across this landscape, while areas dominated by non-wetland grasslands have thinner soils with lower water retention capacity [33,34,38,39].

The climatic conditions correspond to a semi-arid high-Andean regime with an average annual precipitation of approximately 861 mm, concentrated mainly between December and March, consistent with the seasonal rainfall pattern of the central Andes. Between May and August, a marked dry season occurs, characterized by monthly precipitation typically below 10 mm and absolute minimum temperatures reaching −11 °C [34,38]. The estimated annual reference evapotranspiration of 1274 mm exceeds the average annual precipitation, indicating a potential water deficit typical of high-Andean systems that rely heavily on the storage capacity of peatlands and aquifers to sustain baseflows. In this context, high-Andean lakes and peatlands take on special importance as natural moisture reservoirs, as they contribute to maintaining baseflows during the dry season and partially mitigate the seasonality of the water regime [37,38,40,41]. The drainage network exhibits a low-order dendritic pattern in the upper reaches, converging toward the Negrillo River, the main channel of the catchment and a tributary of the hydrological system of the Colca River [29,30]. The Negrillo River has an average annual flow of 2.2 m^3/s, although with marked seasonal low-flow conditions, reflecting strong hydrological seasonality and high dependence on natural mechanisms of water storage and gradual release [37,40,41].

In this context, the Pañe reservoir contributes approximately 57% of the total water supply to the city of Arequipa through the 77.5-km Pañe-Sumbay diversion canal [29,31,42,43]. Its operation is essential to sustain the consumption of over one million inhabitants and to support strategic economic activities such as intensive livestock farming, mining, and hydroelectric power generation in the downstream Chili-Majes-Camaná valley system [29–31,43]. However, this system faces growing constraints associated with increased anthropogenic pressure on water resources and water quality deterioration due to eutrophication [42,43]. These pressures are intensifying in a context where water demand is projected to double by 2050 [29,31,42]. Compounding these challenges is the advanced deterioration of more than 80% of the canal infrastructure, which causes annual water losses of approximately 14 million m^3 due to seepage and leakage [29–31].

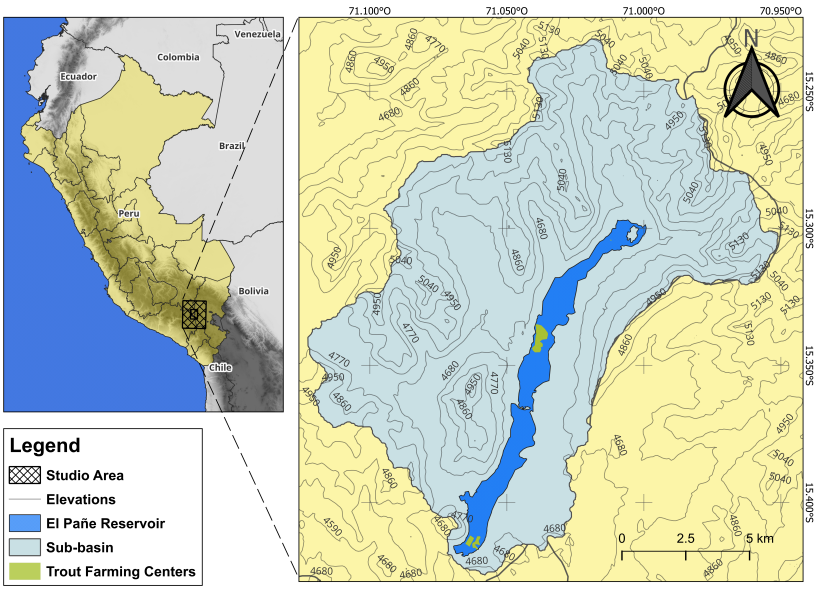


Figure 1. Study area of the Pañe Reservoir located in the high Andes of southern Peru. The map shows the catchment boundaries (gray lines), the reservoir (blue) and trout farming centers (green). Elevation contours are shown in meters above sea level. The inset map of Peru indicates the location of the study area.

2.2. Data Collection and Sources Using Google Earth Engine

The data used in this study were obtained through the Google Earth Engine (GEE) platform, which provided centralized access to multiple global data repositories. The datasets used in this study are summarized in Table 1. Such as precipitation data from the CHIRPS (Climate Hazards Group InfraRed Precipitation with Station data), widely used in hydrological studies of the Peruvian Andes due to its high spatiotemporal resolution and effective performance in mountain catchments. Maximum and minimum temperatures were obtained from the ERA5-Land atmospheric reanalysis product of the European Centre for Medium-Range Weather Forecasts (ECMWF). Land use and land cover (LULC) data were obtained from the MODIS MCD12Q1 product, using the classification scheme of the International Geosphere-Biosphere Programme (IGBP). Soil texture for the 0–30 cm surface layer was obtained from OpenLandMap and classified according to the USDA system, providing information for representing infiltration capacity and water retention in the distributed Curve Number parameterization.

The reservoir design parameters incorporated into the model included a dead storage volume of 41.00×10^6 m^3, a total storage volume of $V_{max} = 148.80 \times 10^6$ m^3 and an active storage capacity of 107.80×10^6 m^3. The simulation was initialized with a total storage volume of 57.80×10^6 m^3. Observed reservoir discharge data (m^3/s) and reservoir stor-

age volume data (m^3) were obtained from the official data portal of AUTODEMA, the institution responsible for the operational management of the Pañe Reservoir, and were used to calibrate and validate the hydrological model. To assess climate change impacts, daily climate projections from the NASA Earth Exchange Global Daily Downscaled Projections for CMIP6 (NEX-GDDP-CMIP6) dataset were employed [44]. This dataset provides statistically downscaled daily climate data at a spatial resolution of 0.25° for the period 2015–2100 under multiple Shared Socioeconomic Pathways (SSPs). Daily precipitation and maximum and minimum temperatures were extracted from the EC-Earth3-Veg-LR, EC-Earth3, and MPI-ESM1-2-LR models under the SSP2-4.5 (moderate emissions) and SSP5-8.5 (high emissions) scenarios.

Table 1. Data sources used in the hydrological modeling of the Pañe Reservoir.

Variable	Source/Product	Resolution	Period
Historical precipitation	CHIRPS v2.0 [45]	0.05°	2009–2020
Historical maximum and minimum temperature	ERA5-Land [46]	0.1°	2009–2020
Future precipitation and temperature	NEX-GDDP-CMIP6 [44]	0.25°	2015–2100
Observed reservoir inflow and storage volume	AUTODEMA [47]	Daily	2010–2019
Land use and land cover	MODIS MCD12Q1 v6.1 [48]	500 m	2020
Surface soil texture	SoilGrids250m [49]	250 m	–

2.3. Hydrological and Reservoir Modeling

The hydrological model was developed as a semi-distributed reservoir water-balance framework to represent the integrated response of the high-Andean catchment at the reservoir scale. The model links spatially distributed runoff generation with Nash-cascade routing and a daily reservoir balance that includes direct precipitation and evaporation over the water surface, seepage losses, observed operational releases, and physical storage limits. This structure allows the catchment response to be translated into reservoir inflow and storage variation, which are the key variables for assessing active-storage trends, critical storage conditions, and operational reliability under future climate and demand scenarios.

Given the scale and data availability of the study area, the model does not explicitly represent several hydrological processes that are characteristic of high-Andean systems, including wetland regulation, temporary groundwater storage, snow-related processes, freeze–thaw dynamics, and delayed subsurface flow. Therefore, the model should be interpreted as a reservoir-scale water-balance framework focused on storage dynamics and operational response, rather than as a fully process-based representation of all catchment hydrological mechanisms.

For the historical simulation, the model was applied over the 2010–2019 period using daily gridded precipitation from CHIRPS and daily reference evapotranspiration (ET_0) estimated with the Hargreaves–Samani equation. Terrain, land-cover, soil, and climate inputs were organized within a common 90-m computational grid in the WGS84 coordinate reference system using the Google Earth Engine platform [13,50]. This spatial framework was used to ensure compatibility among datasets within the modeling workflow, without implying that the native climatic information from CHIRPS or CMIP6 was physically refined to 90 m. Therefore, runoff generation and reservoir-storage simulations were interpreted at the catchment–reservoir scale, considering the native resolution of the climate datasets.

2.3.1. SCS-CN Model

The SCS-CN method estimates daily direct runoff Q based on effective precipitation P and a soil moisture-dependent retention parameter S using the equation [51]:

$$Q = \begin{cases} \dfrac{(P - I_a)^2}{P - I_a + S} & \text{if } P > I_a, \\ 0 & \text{if } P \leq I_a, \end{cases} \tag{1}$$

where $I_a = \lambda S$ represents the initial storage capacity and λ corresponds to an empirical coefficient that controls the fraction of potential storage capacity consumed before runoff begins. The standard value $\lambda = 0.2$ was adopted as the initial reference. The storage parameter is related to the dimensionless Curve Number CN by Jain et al. [51]:

$$S = \frac{25400}{\mathrm{CN}} - 254 \qquad [\mathrm{mm}] \tag{2}$$

The treatment of antecedent soil moisture was based on the three-class antecedent moisture condition (AMC) scheme implemented in the spatially distributed SCS-CN runoff algorithm developed by Jain et al. [51]. In this approach, the five-day antecedent precipitation (P_5) is used to update, on a daily basis at the pixel level, the potential maximum retention (S) that governs direct runoff generation. Accordingly, each grid cell in the catchment is classified as dry (AMC-I), normal (AMC-II), or wet (AMC-III) based on the antecedent rainfall thresholds defined in that scheme:

$$S_{\mathrm{ef}} = \begin{cases} S_1 = f_{s1}\, S_2 & \text{if } P_5 \leq 13 \text{ mm} \quad (\text{AMC-I, dry}), \\ S_2 & \text{if } 13 < P_5 \leq 28 \text{ mm} \quad (\text{AMC-II, normal}), \\ S_3 = f_{s3}\, S_2 & \text{if } P_5 > 28 \text{ mm} \quad (\text{AMC-III, wet}), \end{cases} \tag{3}$$

where S_2 represents potential water retention under average moisture conditions, while S_1 and S_3 correspond to dry and wet conditions, respectively. The factors f_{s1} and f_{s3} were incorporated as scaling coefficients subject to calibration, with initial values of $f_{s1} = 1.3$ and $f_{s3} = 1.4$, in order to adjust the hydrological response of the AMC model to the specific characteristics of the study catchment. The transition between moisture conditions was also based on the standard relationships of the SCS-CN method to convert the mean curve number (CN_2) into its equivalents for dry (CN_1) and wet (CN_3) conditions, following the formulation reported by Jain et al. [51]:

$$\mathrm{CN}_1 = \frac{\mathrm{CN}_2}{2.281 - 0.0128\,\mathrm{CN}_2}, \tag{4}$$

$$\mathrm{CN}_3 = \frac{\mathrm{CN}_2}{0.427 + 0.00573\,\mathrm{CN}_2}. \tag{5}$$

The CN_2 reference values were assigned on a pixel-by-pixel basis by cross-referencing the MCD12Q1 (MODIS) land-cover layer with the ISRIC soil-texture classification mapped to four hydrological groups (A–D) [51]. This distributed approach, in which each raster cell carries its own CN and S values, is consistent with the semi-distributed strategy reported for other basins in Arequipa and with national-scale hydrological modeling efforts for Peru [13,29,52].

The precipitation input used in the SCS-CN calculation was scaled by the calibrated factor k_{effP} before runoff generation. This factor was incorporated to improve the representation of effective precipitation contributing to runoff at the catchment scale, considering high-Andean precipitation variability and the limitations of gridded precipitation products

in complex terrain. Thus, k_{effP} was treated as an effective calibration parameter within the rainfall–runoff component of the model. From this, the average runoff series generated in the catchment was routed to the reservoir via a Nash cascade consisting of n identical linear reservoirs, each characterized by a storage constant K (days):

$$q_t = \alpha\, q_{t-1} + (1-\alpha)\, r_t, \qquad \alpha = e^{-1/K}, \tag{6}$$

where r_t represents the inflow runoff and q_t the time-varying response. By successively applying this relationship over n stages, it was possible to reproduce a hydrograph with a time lag and progressive attenuation.

2.3.2. Reservoir Operation Simulation

The daily water balance for the Pañe reservoir was calculated using a mass conservation equation in a sequential format:

$$V_t = V_{t-1} + V_{\mathrm{run},t} + V_{\mathrm{clim},t} - D_t - V_{\mathrm{seep},t}, \tag{7}$$

where V_t is the reservoir storage volume at the end of day t (m^3), V_{t-1} is the storage volume at the end of the previous day (m^3), $V_{\mathrm{run},t}$ is the routed surface-runoff volume entering the reservoir (m^3), $V_{\mathrm{clim},t}$ represents the net climatic exchange over the reservoir water surface (m^3), D_t is the prescribed daily reservoir release or demand withdrawal (m^3), and $V_{\mathrm{seep},t}$ corresponds to seepage losses from the reservoir (m^3). During the historical period, D_t was derived from observed operating records, whereas in future simulations it was adjusted according to the evaluated demand scenarios. The effective routed-runoff volume contributing to reservoir storage was expressed as:

$$V_{\mathrm{run},t} = q_t\,(A_c - A_{\mathrm{res},t}), \tag{8}$$

where q_t is the routed daily runoff depth reaching the reservoir after Nash-cascade routing (m/day), $A_c = 196.20 \times 10^6$ m^2 is the total catchment area, and $A_{\mathrm{res},t}$ is the variable reservoir surface area on day t (m^2). The reservoir surface area was estimated from the elevation–area–volume polynomial curve:

$$A_{\mathrm{res}}(V) = a_4 V^4 - a_3 V^3 + a_2 V^2 - a_1 V + a_0 \quad [\times 10^6\ \mathrm{m}^2], \tag{9}$$

where V is the volume expressed in m^3 and the adjusted coefficients are $a_4 = 8.919 \times 10^{-8}$, $a_3 = 3.466 \times 10^{-5}$, $a_2 = 3.919 \times 10^{-3}$, $a_1 = 3.065 \times 10^{-2}$ and $a_0 = 2.023$. The net climate exchange across the free surface of the reservoir is calculated as:

$$V_{\mathrm{clim},t} = \left(P_{\mathrm{res},t} - k_{\mathrm{ET}}\,\mathrm{ET}_t\right) \bar{A}_i, \tag{10}$$

where $P_{\mathrm{res},t}$ and ET_t are the average daily precipitation and evapotranspiration over the reservoir surface, calculated using the Hargreaves–Samani formula based on ERA5-Land temperature grids, k_{ET} acts as a calibration factor for evaporation, and $\bar{A}_i = \frac{1}{2}(A_{\mathrm{res},t-1} + A_{\mathrm{res},t})$ is the average reservoir area. Seepage loss is parameterized as:

$$V_{s,t} = k_{\mathrm{fil}}\, V_{s,\mathrm{ref}}\, \bar{A}_i, \tag{11}$$

where $V_{s,\mathrm{ref}}$ (m/d) is the reference specific filtration rate and k_{fil} is a calibration factor. The physical constraints of the system were enforced at each time step. In this study, V_t represents the total storage volume of the reservoir. When V_t exceeds the maximum operating storage volume, $V_{\max} = 148.80 \times 10^6$ m^3, the excess volume is released through the spillway.

Conversely, when V_t falls below the dead storage volume, $V_{dead} = 41.00 \times 10^6$ m^3, water delivery is restricted and the reservoir volume is maintained at this minimum threshold.

The usable or active storage volume was calculated as the storage available above the dead storage level:

$$V_{act,t} = V_t - V_{dead}, \quad (12)$$

where $V_{act,t}$ is the active storage available for reservoir operation. Operational critical conditions were assessed based on the active storage volume. A critical day was defined as a day on which $V_{act,t}$ decreased below the active-storage threshold of $V_{crit,act} = 19.00 \times 10^6$ m^3. This threshold represents a low usable-storage condition within the operating range of the reservoir [13,23,38].

2.3.3. Calibration and Validation Using Genetic Algorithm Optimization

Model calibration was performed for 2010–2016 and independent validation was conducted for 2017–2019. A Genetic Algorithm (GA) was used to search the parameter space associated with runoff generation, flow routing, and reservoir water balance. This approach is well suited for navigating the nonlinear and multimodal parameter space characteristic of coupled hydrological systems. The objective function was defined as a weighted combination of three performance metrics recommended by Moriasi et al. [53,54]: the Nash–Sutcliffe efficiency (NSE), the coefficient of determination (R^2) and the normalized root mean square error (RMSE$_n$).

$$\text{Fitness} = -\text{RMSE}_n + 0.85 \cdot \text{NSE} + 0.05 \cdot R^2 \quad (13)$$

The assigned coefficients define a performance hierarchy among the three metrics. RMSE$_n$ penalizes magnitude errors, NSE receives the highest positive weight because it evaluates model efficiency relative to observed variability, and R^2 receives a lower weight because of its limitations as a standalone performance metric [53,54]. An explicit penalty for negative NSE values was included to avoid low-skill solutions. The GA was initialized with randomly generated parameter sets within the predefined ranges, and new solutions were produced through crossover and mutation operators. Selection was performed using a tournament scheme while preserving an elite subset of the best individuals.

$$\text{NSE} = 1 - \frac{\sum_{t=1}^{N} \left(Q_{obs}^t - Q_{sim}^t\right)^2}{\sum_{t=1}^{N} \left(Q_{obs}^t - \overline{Q}_{obs}\right)^2} \quad (14)$$

$$R^2 = \left(\frac{\sum_{t=1}^{N} \left(Q_{obs}^t - \overline{Q}_{obs}\right)\left(Q_{sim}^t - \overline{Q}_{sim}\right)}{\sqrt{\sum_{t=1}^{N} \left(Q_{obs}^t - \overline{Q}_{obs}\right)^2} \cdot \sqrt{\sum_{t=1}^{N} \left(Q_{sim}^t - \overline{Q}_{sim}\right)^2}} \right)^2 \quad (15)$$

$$\text{RMSE}_n = \frac{\text{RMSE}}{\sigma_{obs}} = \frac{\sqrt{\frac{1}{N}\sum_{t=1}^{N} \left(Q_{obs}^t - Q_{sim}^t\right)^2}}{\sqrt{\frac{1}{N}\sum_{t=1}^{N} \left(Q_{obs}^t - \overline{Q}_{obs}\right)^2}} \quad (16)$$

2.4. Bias Correction and Future Climate Scenarios

The raw outputs of global climate models (GCMs) exhibit systematic biases that limit their direct application in hydrological studies [55]. Bias correction was therefore applied to

the precipitation and maximum and minimum temperature series from the selected CMIP6 models using the Quantile Delta Mapping (QDM) method. This technique allows the simulated distribution to be adjusted relative to the observed reference without altering the projected change signal at each quantile [56,57]. In the case of precipitation, the correction was expressed as:

$$\hat{x}_{\tau}^{\text{proy}} = F_{\text{obs,hist}}^{-1}\left[F_{\text{mod,hist}}\left(x_{\tau}^{\text{proy}}\right)\right] \cdot \frac{x_{\tau}^{\text{proy}}}{F_{\text{mod,hist}}^{-1}\left[F_{\text{mod,hist}}\left(x_{\tau}^{\text{proy}}\right)\right]} \quad (17)$$

where $F_{\text{obs,hist}}^{-1}$ is the inverse cumulative distribution function (CDF) of the observed historical record and $F_{\text{mod,hist}}$ is the CDF of the historical model simulation. This formulation preserves the multiplicative delta change signal across all quantiles, a fundamental property for capturing changes in precipitation extremes under future scenarios [57,58].

The bias correction of climatic variables was performed on a spatially distributed basis, independently for each grid cell and calendar month. For precipitation, a drizzle correction was first applied using a 0.5 mm/day threshold, where values below this limit were classified as dry days prior to the quantile mapping procedure. CHIRPS v2.0 was used as the reference dataset for precipitation, while ERA5-Land reanalysis data were used as reference for maximum and minimum temperatures over the 1985–2014 period. The MPI-ESM1-2-LR, EC-Earth3-Veg-LR, and EC-Earth3 models were selected based on previous studies that evaluated their ability to represent regional climate conditions over Peru, particularly precipitation variability in the Andes. These studies reported coefficients of determination above 0.5 ($R^2 > 0.5$) for precipitation and its seasonal cycle when compared with CHIRPS v2.0 over the 1985–2014 period. The selection was therefore based on demonstrated regional performance rather than on sampling the full spread of the CMIP6 ensemble. Accordingly, the resulting projections should be interpreted as conditional on this reduced performance-based subset. Future projections were generated under the SSP2-4.5 and SSP5-8.5 scenarios.

Water-demand scenarios were developed based on the 2010–2019 historical reservoir discharge series, which reflects the observed seasonal pattern of reservoir operation. A three-year base cycle was established by calculating the conditional average of non-zero discharge values in consecutive historical blocks (2010–2012, 2013–2015, and 2016–2018). This three-year period was used to obtain a representative operational demand pattern, reducing the influence of anomalous individual years while preserving the intra-annual seasonality of water releases. The resulting base cycle was repeated through 2100 as a reference operational pattern and adjusted using annual linear factors representing cumulative demand increases of 50% and 100% by 2080. This procedure preserved the observed seasonal structure of reservoir operation and provided a consistent demand framework for progressively increasing withdrawals under future climate scenarios.

A complementary hydroclimatic diagnostic analysis was conducted to relate projected precipitation patterns to reservoir storage response. Monthly accumulated precipitation was evaluated for three future periods and compared with simulated active storage under the baseline, +50%, and +100% demand scenarios. The maximum 5-day accumulated precipitation (Rx5day), maximum 10-day accumulated precipitation (Rx10day), and consecutive dry days (CDD) indices were calculated from the bias-corrected daily precipitation series to assess changes in multi-day precipitation extremes and dry-spell duration.

3. Results

3.1. Hydrological Model Performance and Spatial Parameterization

The genetic algorithm showed a gradual improvement in population performance over the 20 generations evaluated. The best fitness value increased from 0.466 in Generation

1 to 0.521 in Generation 13 with no further significant improvements during the remaining generations. This behavior indicates that the search process converged toward a dominant solution within the explored parameter space. The selected configuration corresponded to the ESC_G13_I6 scenario, associated with individual 6 of Generation 13, and was adopted as the final parameterization for historical and future simulations.

The calibrated model reproduced the observed storage dynamics of the Pañe Reservoir during both calibration and validation periods (Figure 2). For the calibration period, the model achieved NSE = 0.886, $R^2 = 0.907$, and $\text{RMSE}_n = 0.337$, indicating good agreement with the observed temporal variability and the main filling and drawdown cycles. During validation, model performance remained similar, with NSE = 0.888, $R^2 = 0.891$, and $\text{RMSE}_n = 0.335$. The small differences between calibration and validation metrics suggest that the selected parameterization maintained stable predictive performance when applied to an independent period, supporting its use for subsequent scenario simulations.

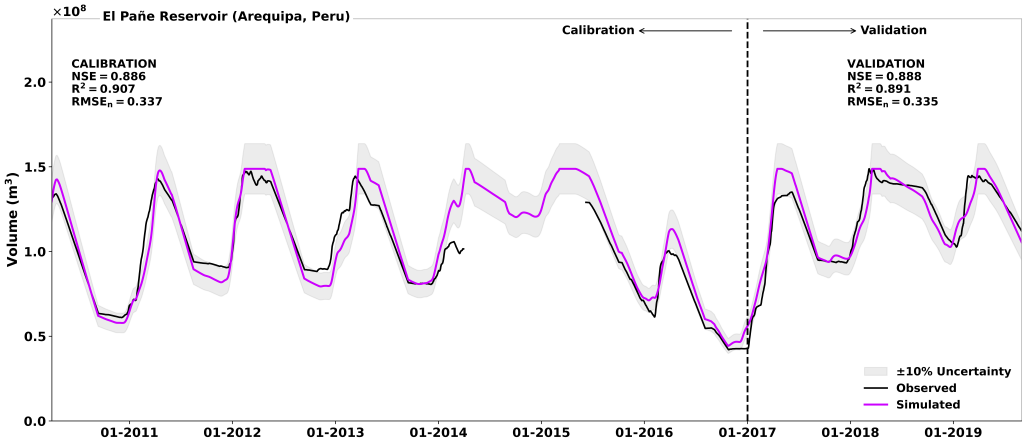


Figure 2. Observed and simulated monthly reservoir storage volume at the Pañe Reservoir (Arequipa, Peru) during the calibration (2010–2016) and validation (2017–2019) periods. The gray shaded area represents a ±10% reference envelope around simulated values.

The spatial parameterization of the Curve Numbers showed high calibrated values for LULC class 10 in both soil groups, whereas LULC class 16 presented a stronger contrast between groups. These values provide a model-effective description of runoff response across land-cover and soil combinations.

Table 2 summarizes the calibrated parameters of the best-performing configuration and their respective search ranges. These values should be interpreted as effective calibration terms used to reproduce the integrated reservoir-scale response within the adopted model structure. The Nash cascade configuration, with $n = 4$ linear reservoirs and $K = 4.31$ days, produced a model-effective routing delay equivalent to approximately 17 days. This routing behavior represents the delay required within the routing component to match the observed reservoir response.

The calibrated balance parameters also acted as empirical adjustment terms within the model structure. The evapotranspiration factor $k_{\text{ET}} = 0.808$ scaled the Hargreaves-based evapotranspiration component, while $V_s = 9.59 \times 10^{-3}$ m/d and $k_{\text{fil}} = 0.695$ contributed to matching the observed reservoir storage dynamics. Similarly, the effective precipitation factor $k_{\text{effP}} = 1.813$ and the runoff scaling factor $k_q = 1.709$ adjusted the rainfall–runoff component under the available forcing data. The initial abstraction coefficient $\lambda_{ia} = 0.039$, lower than the conventional SCS-CN reference value of 0.2, suggests that a low abstraction value was required within the model formulation to reproduce the observed response. Overall, the calibrated parameter set provides a model-effective representation of the catchment–reservoir response within the adopted model structure.

Table 2. Calibrated parameter values for the best-performing hydrological model configuration at the Pañe Reservoir. The selected configuration corresponds to scenario ESC_G13_I6 and summarizes the final parameter set adopted for the historical simulation and subsequent climate–demand scenario analysis.

Parameter	Description	Search Range	Selected Value
n	Number of linear reservoirs in the Nash cascade	2–6	4
K	Nash routing coefficient	2.00–10.00	4.313
k_{fil}	Infiltration scaling factor	0.20–1.50	0.695
k_{ET}	Evapotranspiration scaling factor	0.60–1.10	0.808
V_s	Seepage scaling parameter	0.000–0.010	0.00959
$CN10_{g7}$	Curve Number for LULC class 10 under soil group 7	80.00–98.00	95.721
$CN16_{g7}$	Curve Number for LULC class 16 under soil group 7	75.00–98.00	85.715
$CN10_{g9}$	Curve Number for LULC class 10 under soil group 9	90.00–98.00	96.316
$CN16_{g9}$	Curve Number for LULC class 16 under soil group 9	45.00–75.00	66.284
k_{effP}	Effective precipitation scaling factor	1.20–1.90	1.813
k_q	Runoff scaling factor	1.00–2.50	1.709
λ_{ia}	Initial abstraction coefficient in the SCS-CN method	0.005–0.250	0.039

Note: LULC = land use and land cover; CN = Curve Number; SCS-CN = Soil Conservation Service Curve Number method.

3.2. Bias-Corrected CMIP6 Climate Projections

Bias correction using QDM-Gamma improved the performance of the three GCMs in reproducing precipitation observed by CHIRPS during the 1985–2014 historical period. The EC-Earth3-Veg-LR showed the most notable improvement, increasing its coefficient of determination from $R^2 = 0.647$ to $R^2 = 0.704$ and reducing the RMSE from 34.2 to 31.3 mm. The MPI-ESM1-2-LR model showed an improvement from $R^2 = 0.621$ to $R^2 = 0.662$, along with a decrease in the RMSE from 35.4 to 33.4 mm, and EC-Earth3 recorded the largest relative gain in R^2, rising from $R^2 = 0.558$ to $R^2 = 0.633$ and reducing its RMSE from 38.3 to 34.8 mm. From the visual analysis, the corrected series more accurately approximated the observed precipitation during the peaks of the wet season (November-April) and the near-zero precipitation characteristic of the dry season (May–October), as shown in Figure 3. Furthermore, the application of QDM-Gamma helped mitigate the overestimates and shifts present in the raw simulations, particularly during higher-intensity events, without substantially altering the seasonal and interannual structure of precipitation.

The three raw GCMs exhibited systematic biases in maximum temperature (T_{max}), with RMSE values exceeding 4.60 °C. Initial biases in minimum temperature (T_{min}) were more moderate, with RMSE values between 1.59 and 1.65 °C. QDM-Normal reduced the RMSE of T_{max} by more than 67% in all models: MPI-ESM1-2-LR decreased from 4.64 to 1.50 °C, EC-Earth3-Veg-LR from 4.60 to 1.38 °C, and EC-Earth3 from 4.94 to 1.50 °C. For T_{min}, the three models converged toward RMSE values between 0.88 and 0.91 °C. As shown in Figure 4, the corrected series reproduced the amplitude and seasonal variability observed in ERA5-Land more closely, reducing the systematic bias of the raw simulations, especially during the dry season.

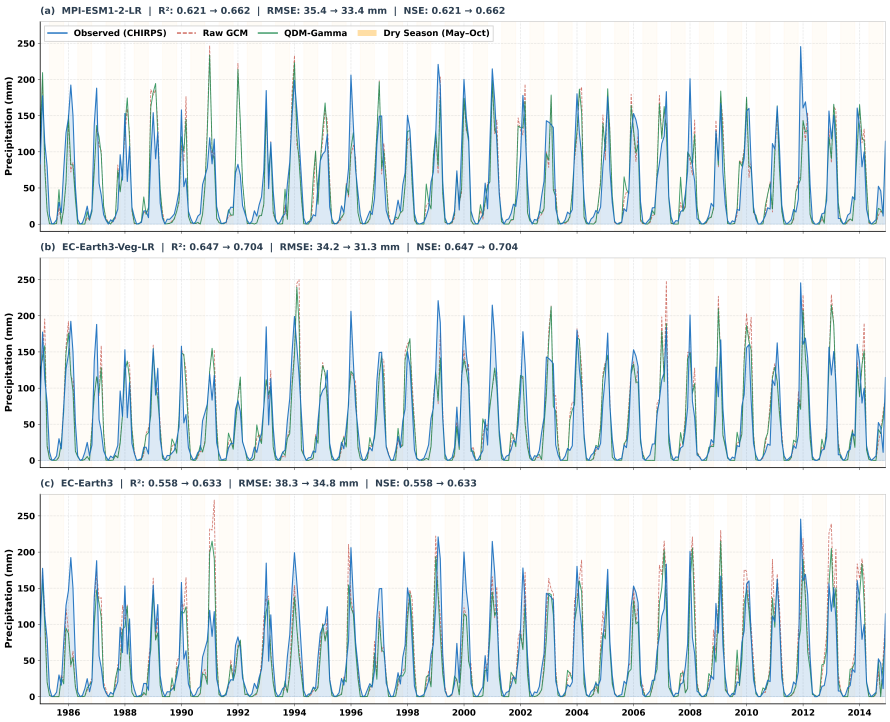


Figure 3. Monthly precipitation time series (1985–2014) for the three CMIP6 models evaluated: (**a**) MPI-ESM1-2-LR, (**b**) EC-Earth3-Veg-LR, and (**c**) EC-Earth3. Each panel shows the observed series from CHIRPS (solid blue line), the raw GCM output (dashed red line), and the QDM-Gamma bias-corrected series (solid green line). Shaded yellow areas indicate the dry season (May–October).

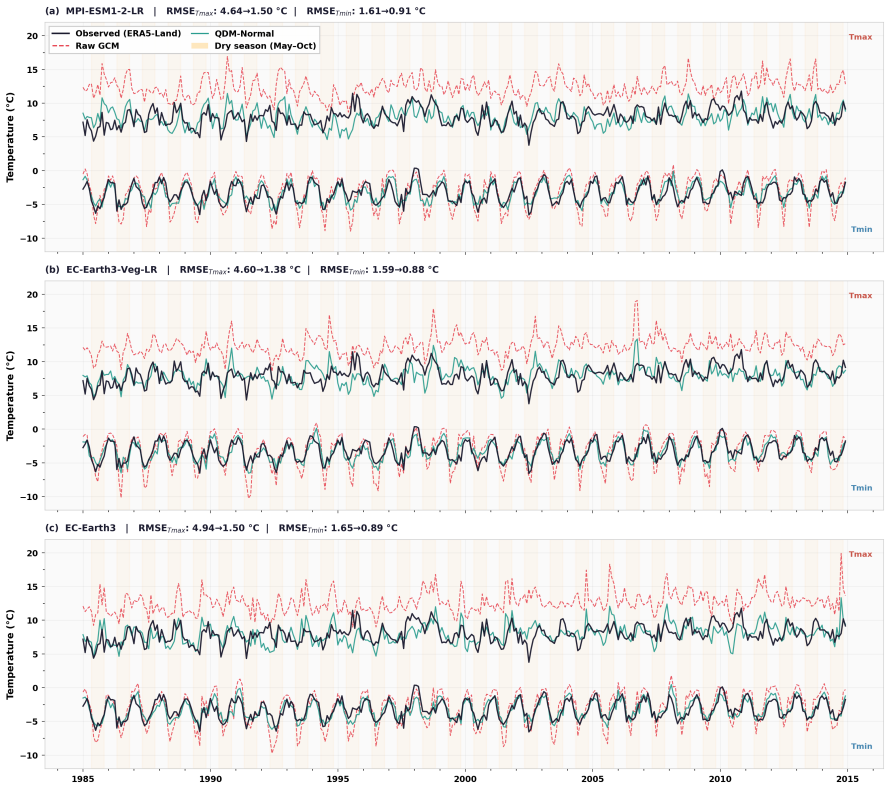


Figure 4. Monthly time series of maximum (T_{max}, upper band) and minimum (T_{min}, lower band) temperature (1985–2014) for the three CMIP6 models evaluated: (**a**) MPI-ESM1-2-LR, (**b**) EC-Earth3-Veg-LR, and (**c**) EC-Earth3. Each panel displays the ERA5-Land observed series (solid black line), the raw GCM output (dashed red line), and the QDM-Normal bias-corrected series (solid teal line). Shaded orange areas indicate the dry season (May–October).

3.3. Reservoir Storage Dynamics Under Climate and Demand Scenarios

Active storage volumes showed marked inter-annual variability during the 2020–2100 period under the evaluated climate and demand scenarios. In the scenario where demand does not grow (ESC 00), corresponding to the baseline condition, storage remained between the medium and high categories (~64–79 $\times 10^6$ m^3). The linear trend was positive in both SSP simulation sets with increases of $+1.307 \times 10^6$ m^3 per decade in Figure 5a and $+2.162 \times 10^6$ m^3 per decade in Figure 6a. In contrast, under the ESC 50 scenario, associated with a 50% increase in demand, values were more frequently concentrated in the medium and low categories with recurring declines to levels near 40–50 $\times 10^6$ m^3. The trend was negative in Figure 5b at -1.453×10^6 m^3 per decade, while in Figure 6b it remained practically stable at -0.002×10^6 m^3 per decade. In the ESC 100 scenario with a 100% increase in demand, the lowest storage volumes were recorded, with a longer duration in the low category and events close to the critical threshold of 19 $\times 10^6$ m^3. The trend was downward in both cases with -2.799×10^6 m^3 per decade in Figure 5c and -1.472×10^6 m^3 per decade in Figure 6c.

The comparison of models revealed differences in annual storage fluctuations. The EC-Earth3 and EC-Earth3-Veg-LR models showed higher values in several periods, while MPI-ESM1-2-LR recorded more pronounced declines, especially in scenarios with higher demand. The three-model mean generally fell within the range across the selected models and revealed an annual pattern of recurring fluctuations with peaks near the high category, while the lowest values fell toward the low or critical category for the ESC 50 and ESC 100 scenarios (Figures 5 and 6).

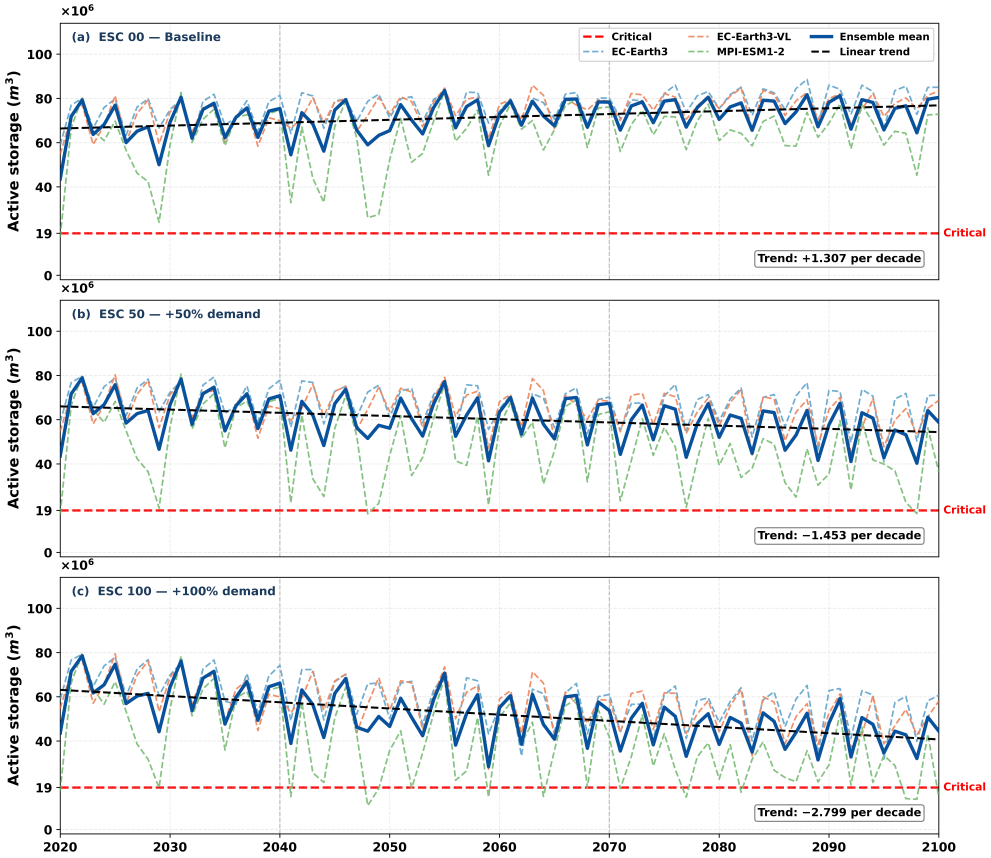


Figure 5. Projected active storage under SSP2-4.5 for the demand scenarios ESC 00, ESC 50, and ESC 100 during the period 2020–2100. (**a**) ESC 00 baseline scenario; (**b**) ESC 50, with a 50% demand increase; (**c**) ESC 100, with a 100% demand increase.

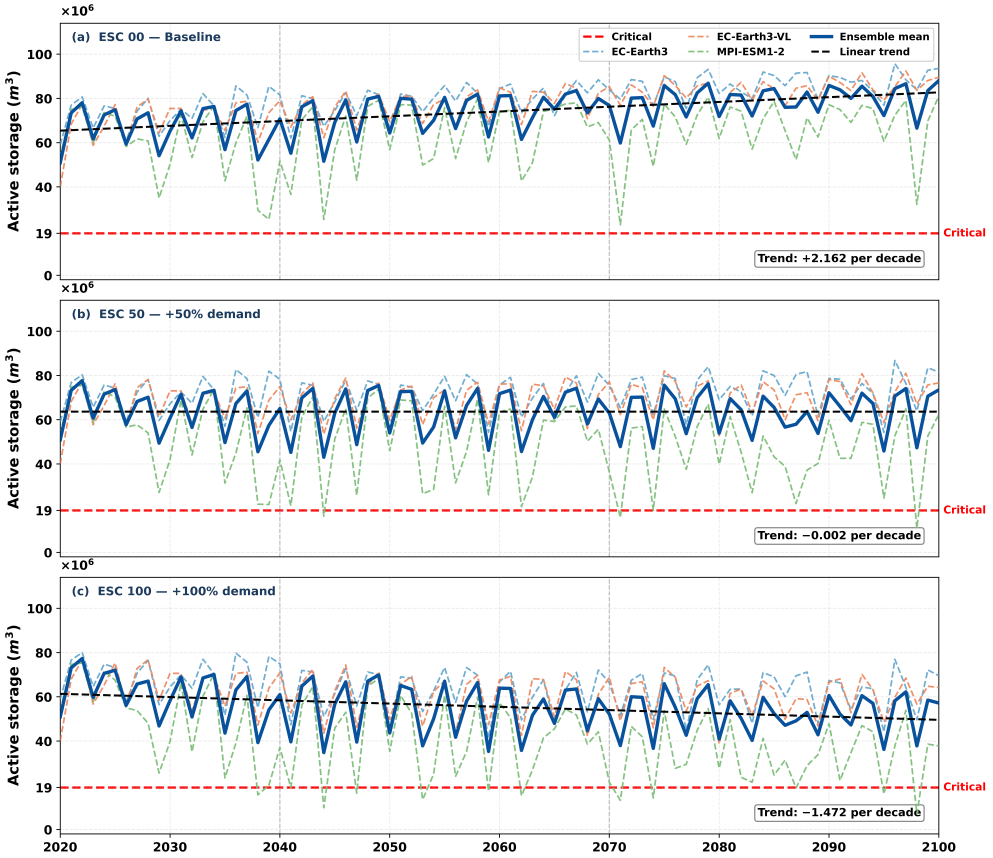


Figure 6. Projected active storage under SSP5-8.5 for the demand scenarios ESC 00, ESC 50, and ESC 100 during the period 2020–2100. (**a**) ESC 00 baseline scenario; (**b**) ESC 50, with a 50% demand increase; (**c**) ESC 100, with a 100% demand increase.

Under the SSP2-4.5 scenario, effective precipitation showed an upward trend of +0.123 mm/day per decade. The three-model average rose from values close to 2.0–2.5 mm/day at the start of the period (2020–2040) to approximately 3.0–3.3 mm/day toward the end of the century. The range across the selected models showed a dispersion of approximately 1.0 to 4.7 mm/day, with maximum values observed around the second half of the analyzed period (2055–2100) (Figure 7a). Under SSP5-8.5, effective precipitation showed a more pronounced increase, with a trend of +0.283 mm/day per decade. In this case, the three-model mean increased from values close to 2.0 mm/day to approximately 4.0–4.8 mm/day by 2100, while the range across the selected models reached values exceeding 7.0 mm/day by the end of the 21st century (Figure 7b). In both scenarios, the model dispersion widens progressively starting in the mid-21st century with the EC-Earth3-VL model projecting the highest values in the high-emission scenario.

Mean annual maximum reservoir surface temperature exhibited pronounced warming trends under both climate scenarios. Under SSP2-4.5, the three-model average increased from values around 8.5–9.0 °C at the beginning of the period to approximately 10.5–11.0 °C by the end of the century, with a trend of +0.271 °C per decade (Figure 7c). Under SSP5-8.5, the increase was greater, with a trend of +0.599 °C per decade. In this scenario, the maximum reservoir temperature rose from values near 8.0–8.5 °C to readings close to 13.0–14.0 °C by 2100, with greater inter-model variability in the final decades (Figure 7d). Inter-model variability is greater under SSP5-8.5, where the EC-Earth3-VL model consistently projects the highest temperatures.

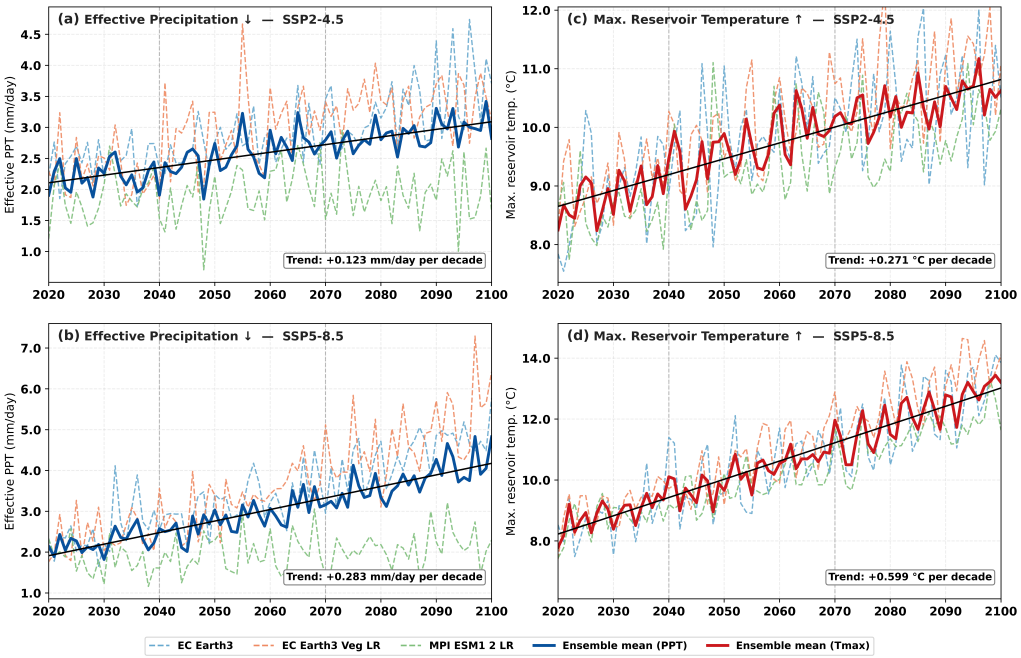


Figure 7. Projected effective precipitation and maximum reservoir temperature under SSP2-4.5 and SSP5-8.5 during the period 2020–2100. (**a**) Effective precipitation under SSP2-4.5; (**b**) effective precipitation under SSP5-8.5; (**c**) maximum reservoir temperature under SSP2-4.5; (**d**) maximum reservoir temperature under SSP5-8.5.

Evapotranspiration from the reservoir showed a gradual increase over the period evaluated. Under SSP2-4.5, the trend was +0.035 mm/day per decade, with three-model mean values ranging from approximately 2.25 to 2.60 mm/day (Figure 8a). Under SSP5-8.5, the trend was +0.072 mm/day per decade, with values increasing from approximately 2.25 mm/day to 2.85–2.90 mm/day toward the end of the century (Figure 8c). In both scenarios, the three selected models exhibited interannual oscillations within the range across the selected models, with greater amplitude under SSP5-8.5.

Under SSP2-4.5, the highest trend was recorded, at +10.2 days/year per decade. The three-model mean showed low values at the beginning of the period and recurring increases starting in the second half of the century, with peaks close to 120–160 critical days per year in some intervals (Figure 8b). Under SSP5-8.5, the trend was also positive, although smaller, at +4.7 days/year per decade. In this scenario, the three-model mean reached approximately 100–125 critical days per year in some periods, while the range across the selected models exceeded 200 critical days per year in certain years (Figure 8d).

The seasonal analysis showed that accumulated precipitation was concentrated mainly between January and April under both SSP2-4.5 and SSP5-8.5, with maximum values in March across the three future periods evaluated (Figure 9a,b). March precipitation increased from approximately 290 to 360 mm under SSP2-4.5 and from approximately 295 to 470 mm under SSP5-8.5 between 2020–2049 and 2071–2100. In contrast, precipitation remained low during the dry season, generally below 30 mm/month from May to October. Active storage reflected this seasonal contrast, with higher values during the wet season and lower values toward the end of the dry season. Under the baseline demand scenario, storage remained above the critical threshold of 19.00 $\times$ 10^6 m^3 throughout the year. Under ESC 50, storage approached the threshold during the dry season, while under ESC 100 the lowest values occurred between September and November, reaching approximately 0–8 $\times$ 10^6 m^3 under SSP2-4.5 and 6–20 $\times$ 10^6 m^3 under SSP5-8.5.

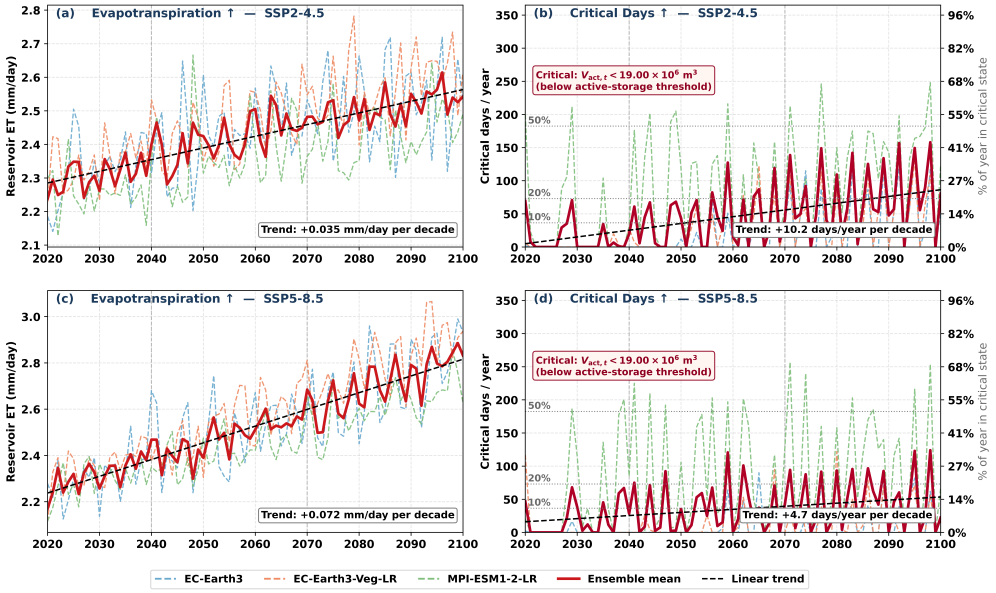


Figure 8. Projected reservoir evapotranspiration and critical days under SSP2-4.5 and SSP5-8.5 during the period 2020–2100. (**a**) Reservoir evapotranspiration under SSP2-4.5; (**b**) critical days under SSP2-4.5; (**c**) reservoir evapotranspiration under SSP5-8.5; (**d**) critical days under SSP5-8.5.

The hydroclimatic extreme indices showed positive trends in maximum multi-day precipitation under both climate scenarios (Figure 9c,d). Under SSP2-4.5, Rx5day and Rx10day increased by +5.43 and +8.78 mm/decade, respectively, while CDD showed a slight decrease of −0.9 days/decade. Under SSP5-8.5, the trends were higher for Rx5day and Rx10day, with increases of +12.13 and +19.42 mm/decade, respectively, while CDD decreased slightly by −0.7 days/decade. These results show an increase in short-duration accumulated precipitation extremes, together with a slight reduction in the maximum duration of consecutive dry days during the 2020–2100 period.

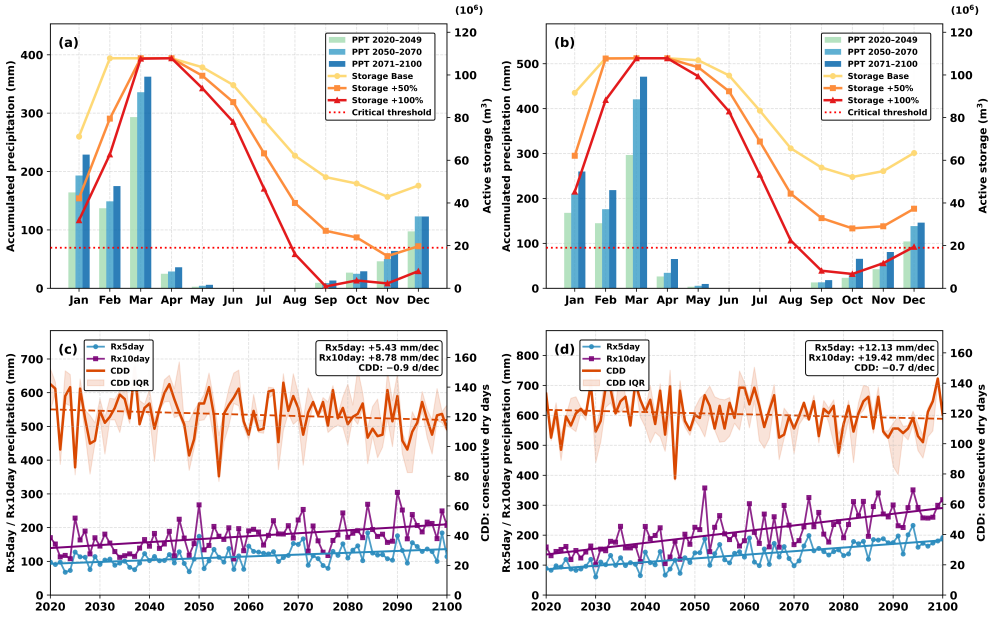


Figure 9. Seasonal accumulated precipitation, active storage, and hydroclimatic extreme indices under SSP2-4.5 and SSP5-8.5. (**a**) Monthly accumulated precipitation and active storage under SSP2-4.5; (**b**) monthly accumulated precipitation and active storage under SSP5-8.5; (**c**) Rx5day, Rx10day, and CDD trends under SSP2-4.5; (**d**) Rx5day, Rx10day, and CDD trends under SSP5-8.5.

4. Discussion

The calibration and validation statistics support the use of the model for analyzing reservoir storage dynamics and relative vulnerability under alternative climate and demand scenarios. However, model performance should not be interpreted as evidence that all dominant high-Andean hydrological processes are explicitly represented. Rather, the model provides an operational approximation of the integrated catchment–reservoir response, consistent with the purpose of evaluating active storage, critical storage conditions, and demand-driven vulnerability. This distinction is important because high-Andean systems involve nonlinear interactions among precipitation seasonality, peatland storage, volcanic aquifers, snow and frost processes, and delayed subsurface contributions that cannot be fully diagnosed from reservoir storage records [37,38,40,41].

A central implication of this modeling strategy is that the SCS-CN component must be interpreted as an empirical runoff-generation module. The SCS-CN method was originally developed to estimate direct runoff from rainfall, land cover, soil condition, and antecedent wetness, and its transfer to volcanic, peatland-influenced, and high-altitude Andean environments involves conceptual simplification [51]. In the study area, runoff generation may also reflect high-Andean processes not explicitly represented in the model, including bofedal saturation, shallow groundwater contributions, fractured volcanic lithology, temporary snow accumulation and melt, and freeze–thaw effects. Therefore, the Curve Number values and the initial abstraction coefficient should be regarded as effective parameters summarizing the net wet-season response of the catchment at the reservoir outlet.

The calibrated precipitation effectiveness factor $k_{\mathrm{effP}} = 1.813$ summarizes the adjustment required to reproduce the historical water balance under the available forcing data. This is consistent with previous studies reporting uncertainties and underestimation of satellite precipitation products in complex Andean topography, where sparse rain-gauge networks, localized convection, and orographic gradients complicate precipitation retrieval [29,31,50]. In this study, k_{effP} aggregates precipitation bias and unresolved hydrological contributions within the model structure, including delayed wetland and groundwater inputs. Because future simulations were generated using a single optimal parameter set, the influence of this large calibrated factor is propagated into the scenario results and should be considered a source of parametric uncertainty.

The calibrated Nash routing parameters, $n = 4$ and $K = 4.313$ days, indicate that the catchment response is delayed and should be interpreted as effective routing parameters rather than as explicit representations of wetland hydraulics, aquifer recession, or snowmelt routing [37,40,41]. This distinction matters because similar storage dynamics may arise from equifinality among precipitation correction, runoff generation, routing delay, and seepage parameters. Thus, the model is best viewed as a semi-distributed reservoir water-balance framework for scenario screening rather than a diagnostic model of individual hydrological processes.

The calibration–validation split also represents an important limitation for interpreting long-term climate impacts. Although the validation period was sufficient to assess recent seasonal reservoir behavior, a short validation window limits the ability to capture interannual variability, extremely wet or dry years, and low-frequency climate anomalies that characterize high-Andean hydrology. This restriction is mainly associated with the limited availability of continuous and reliable hydrometeorological information in the catchment, a common condition in high-altitude Andean systems with sparse monitoring networks. As a result, predictive confidence is lower under extreme wet and dry conditions, and the scenario outputs should be interpreted as plausible vulnerability trajectories rather than robust forecasts of reservoir storage to 2100. Consequently, while the model is useful for identifying trends, critical thresholds, and operational stress conditions, its behavior under

hydrological extremes remains uncertain and should be strengthened in future research through longer observed records and additional hydrological monitoring.

The climate projections show that increasing precipitation does not necessarily translate into lower vulnerability. Under both SSP2-4.5 and SSP5-8.5, projected precipitation increases are concentrated mainly during the wet season and are accompanied by rising Rx5day and Rx10day indices. This pattern suggests a tendency toward more episodic water inputs, where part of the additional precipitation may occur during periods when the reservoir and natural storage components already have limited capacity to retain water. In high-Andean systems, this distinction is hydrologically important because dry-season water security depends less on annual precipitation totals than on the capacity of wetlands, aquifers and reservoirs to transform wet-season inputs into delayed baseflow and regulated storage [37,40,41]. Therefore, the projected increase in effective precipitation should be interpreted as a potential opportunity for wet-season capture, but not as automatic evidence of improved dry-season reliability.

The projected warming reinforces this interpretation. Maximum reservoir surface temperature increases by approximately +0.271 °C per decade under SSP2-4.5 and +0.599 °C per decade under SSP5-8.5. These trends increase evaporative demand and may reduce the net storage benefit of higher precipitation, particularly during transition and dry-season months when inflows decline and surface losses become more relevant. Comparable climate-impact studies in mountain and reservoir systems have shown that warming can offset part of the apparent hydrological gains from increased precipitation by intensifying evapotranspiration and altering seasonal water availability [7,12,59]. In the Pañe system, this helps explain why SSP5-8.5, despite projecting higher precipitation than SSP2-4.5, does not eliminate the occurrence of critical storage conditions under increased demand.

The demand scenarios reveal that the main driver of future vulnerability is not climate forcing alone, but the interaction between climate variability, reservoir regulation and increasing withdrawals. Under ESC 00, active storage remains generally within medium to high categories and shows positive trends, indicating that the projected hydroclimatic supply would be sufficient to sustain current operating conditions. Under ESC 50, the system becomes more sensitive to interannual variability, with more frequent declines toward 40–50 $\times 10^6$ m^3 of active storage. Under ESC 100, the reservoir approaches the active-storage critical threshold with increasing recurrence after approximately 2060–2065. This behavior indicates a reduction in operational reliability: once demand approaches or exceeds the effective regulatory capacity of the catchment–reservoir system, small differences in wet-season recharge, evaporation or release timing can produce disproportionately large increases in low-storage duration [2,6,9].

For this reason, the number of critical days provides a more management-relevant vulnerability indicator than mean annual precipitation or mean annual storage alone. The increase in critical days under both SSPs indicates that the reservoir may experience longer periods with limited active reserve, even in scenarios where annual precipitation trends are positive. The apparently stronger critical-day trend under SSP2-4.5 compared with SSP5-8.5 can be explained by the smaller wet-season precipitation increase projected under the moderate-emission pathway, which provides less buffering against rising demand. However, the high-emission scenario still produces severe individual years, with model members reaching more than 200 critical days in some periods. This result highlights the importance of evaluating not only average trajectories but also the duration and recurrence of low-storage states, because prolonged active-storage depletion can reduce operational flexibility, delay recovery before the following dry season and increase dependence on emergency demand restrictions or complementary sources [9,21].

The ecohydrological implications extend beyond reservoir volume. Bofedales and high-Andean wetlands regulate dry-season flow through temporary storage and delayed release, but their buffering capacity depends on maintaining saturated peat and hydraulic connectivity with contributing hillslopes and shallow groundwater systems [36,40,41]. Prolonged periods of low reservoir storage may therefore coincide with broader catchment water stress, reducing the capacity of wetlands to sustain baseflow during the dry season. The present model cannot explicitly simulate peatland degradation, changes in hydraulic porosity or groundwater–wetland feedbacks; nevertheless, the projected increase in low-storage duration suggests that these processes should be considered in adaptation planning. Ignoring them may underestimate vulnerability, because degradation of natural storage would reduce the very delayed-flow mechanisms that currently help stabilize reservoir inflows.

Water quality represents an additional potential risk pathway. The projected warming of the reservoir, together with lower active-storage conditions under high demand, may create conditions that could be more favorable to water-quality deterioration. This may include longer water-retention periods and greater nutrient concentration, although the development of algal or cyanobacterial blooms was not explicitly assessed in this study. This concern is consistent with previous evidence of eutrophication risk in the Pañe system and with broader findings that reservoir vulnerability under climate change is not limited to volumetric scarcity. However, because the present study does not include ecological or limnological modeling, these implications should be interpreted as plausible risks rather than expected outcomes. Under this interpretation, the co-occurrence of higher temperature and lower active storage highlights a compound-risk pathway that warrants future monitoring and targeted water-quality assessment.

5. Conclusions

The results suggest that adaptation should prioritize operational flexibility and demand management rather than relying solely on projected increases in precipitation. Measures such as revising release rules, incorporating early-warning indicators based on active storage and critical-day frequency, reducing conveyance losses in the Pañe–Sumbay canal, protecting bofedales, and expanding complementary wet-season storage would directly address the mechanisms identified by the simulations. These actions are consistent with international reservoir-adaptation approaches that combine climate-informed operating rules, infrastructure efficiency and nature-based regulation to increase resilience under uncertain future inflows [9,21,22]. In the Pañe case, such measures are particularly relevant because demand growth produces vulnerability even when climate projections indicate stable or increasing precipitation.

Several limitations should be noted. The hydrological model does not explicitly resolve snow accumulation and melt, freeze–thaw effects, peatland hydraulics, groundwater storage, land-cover change, or water-quality processes. In addition, the simulations rely on a single optimal parameter set, and parameter uncertainty or sensitivity was not formally quantified. This limitation is particularly relevant for k_{effP}, whose large calibrated value affects the historical water balance and conditions future storage projections. The independent validation period, 2017–2019, was short, which limits confidence under extreme wet and dry conditions. QDM bias correction improves agreement with the historical reference period but cannot remove uncertainty associated with future climate states outside the observed range [57,58,60]. Future work should incorporate longer in situ precipitation and inflow records, snow and wetland monitoring, groundwater observations, sensitivity and uncertainty analysis, higher-resolution regional climate information, and coupled quantity–quality modeling.

Author Contributions: Conceptualization, F.d.L.A.C. and J.A.C.M.; methodology, F.d.L.A.C., R.I.G.M. and R.M.M.S.; software, F.d.L.A.C. and R.I.G.M.; validation, F.d.L.A.C., S.L.A. and J.P.-A.; formal analysis, F.d.L.A.C. and R.I.G.M.; investigation, F.d.L.A.C., S.A.Z.M. and R.M.M.S.; hydrological modeling, F.d.L.A.C., R.I.G.M. and R.M.M.S.; meteorological data analysis, F.d.L.A.C., S.A.Z.M. and S.L.A.; climate scenario analysis, F.d.L.A.C. and J.P.-A.; remote sensing and GEE implementation, F.d.L.A.C. and R.I.G.M.; writing—original draft preparation, F.d.L.A.C. and J.A.C.M.; writing—review and editing, R.I.G.M., S.L.A. and J.P.-A.; visualization, F.d.L.A.C. and R.I.G.M.; supervision, R.M.M.S. and J.P.-A.; project administration, J.A.C.M. and R.M.M.S. All authors have read and agreed to the published version of the manuscript.

Funding: This research received no external funding.

Institutional Review Board Statement: Not applicable.

Data Availability Statement: The data, source code, and materials generated and used in this study for the HydroBalance-GEE project are publicly available to ensure transparency and reproducibility. The full project repository, including all scripts, model configurations, and documentation, can be accessed at GitHub: https://github.com/reyc43541-ops/HydroBalance-GEE (accessed on 15 January 2026). Any additional files, datasets, or experimental outputs produced during the study are included within the repository. Users can reproduce the analyses and run the models directly from the provided scripts and resources. No sensitive or private data were used in this study.

Acknowledgments: The authors would like to acknowledge the valuable support of the Autonomous Authority of Majes (AUTODEMA) for facilitating access to the Pañe reservoir and providing hydrological and operational data essential for this study. The authors reviewed and edited the generated content and take full responsibility for the content of this publication.

Conflicts of Interest: The authors declare no conflicts of interest. This research received no external funding, and no institution or sponsor had any role in the design of the study; the collection, analysis, or interpretation of data; the writing of the manuscript; or the decision to publish the results.

Abbreviations

The following abbreviations are used in this manuscript:

GCM	Global Climate Model
CMIP6	Coupled Model Intercomparison Project Phase 6
SSP	Shared Socioeconomic Pathway
QDM	Quantile Delta Mapping
NSE	Nash–Sutcliffe Efficiency
$RMSE_n$	Normalized Root Mean Square Error
ET	Evapotranspiration
LULC	Land Use and Land Cover
SCS-CN	Soil Conservation Service Curve Number
AMC	Antecedent Moisture Condition
GEE	Google Earth Engine
CHIRPS	Climate Hazards Group InfraRed Precipitation with Station data
Rx5day	Maximum 5-day accumulated precipitation
Rx10day	Maximum 10-day accumulated precipitation
CDD	Consecutive Dry Days

References

1. Amparo-Salcedo, M.; Pérez-Gimeno, A.; Navarro-Pedreño, J. Water Security Under Climate Change: Challenges and Solutions Across 43 Countries. *Water* **2025**, *17*, 633. [CrossRef]
2. Sýs, V.; Fošumpaur, P.; Kašpar, T. The Impact of Climate Change on the Reliability of Water Resources. *Climate* **2021**, *9*, 153. [CrossRef]

3. Ferreira, G.W.D.S.; Reboita, M.S.; Ribeiro, J.G.M.; Souza, C.A.D. Assessment of Precipitation and Hydrological Droughts in South America through Statistically Downscaled CMIP6 Projections. *Climate* **2023**, *11*, 166. [CrossRef]
4. Silva, N.O.D.; Rocha, R.P.D.; Nunes, A.M.P. Unraveling the coupled HighResMIP-CMIP6 models resolution impacts in present climate and future projections of water availability over South America. *Front. Earth Sci.* **2025**, *13*, 1537081. [CrossRef]
5. Biglarbeigi, P.; Strong, W.A.; Finlay, D.; McDermott, R.; Griffiths, P. A Hybrid Model-Based Adaptive Framework for the Analysis of Climate Change Impact on Reservoir Performance. *Water Resour. Manag.* **2020**, *34*, 4053–4066. [CrossRef]
6. Silva, M.V.M.D.; Lima, C.E.S.; Silveira, C.D.S. Impact of Climate Change and Consumptive Demands on the Performance of São Francisco River Reservoirs, Brazil. *Climate* **2023**, *11*, 89. [CrossRef]
7. Ding, Z.; Angarita, H.; Cáceres, C.A.M.; Lavado-Casimiro, W.; Goldstein, J.A.; Batista, N.; Wu, T.; Fisher, D.; Farah, A.B.; Zheng, H.; et al. Sustainable land and irrigation management to limit loss of hydropower in the Andes-Amazon headwaters. *Commun. Earth Environ.* **2024**, *5*, 648. [CrossRef]
8. Granados, A.; Sordo-Ward, A.; Paredes-Beltrán, B.; Garrote, L. Exploring the Role of Reservoir Storage in Enhancing Resilience to Climate Change in Southern Europe. *Water* **2021**, *13*, 85. [CrossRef]
9. Beça, P.; Rodrigues, A.C.; Nunes, J.P.; Diogo, P.; Mujtaba, B. Optimizing Reservoir Water Management in a Changing Climate. *Water Resour. Manag.* **2023**, *37*, 3423–3437. [CrossRef]
10. Tayyeh, H.K.; Mohammed, R. Vulnerability and resilience of hydropower generation under climate change scenarios: Haditha dam reservoir case study. *Appl. Energy* **2024**, *366*, 123308. [CrossRef]
11. Quenta-Herrera, E.; Crespo-Pérez, V.; Mark, B.G.; Gonzales, A.L.; Kulonen, A. Mountain freshwater ecosystems and protected areas in the tropical Andes: Insights and gaps for climate change adaptation. *Environ. Conserv.* **2022**, *49*, 17–26. [CrossRef]
12. Saavedra, D.; Montesinos, C.A.; Lavado-Casimiro, W.S. Impacts of land use and climate changes on hydrological responses in a Peruvian Andean watershed. *J. Water Clim. Change* **2025**, *16*, 2111–2133. [CrossRef]
13. Quiroz, J.A.; Garcia-Chevesich, P.A.; Martínez, G.; Martínez, K.; Tejada-Purizaca, T.; Murray, K.E.; McCray, J.E. Water Resources Evaluation and Sustainability Considering Climate Change and Future Anthropic Demands in the Arequipa Region of Southern Peru. *Sustainability* **2023**, *15*, 16270. [CrossRef]
14. Botero, B.A.; Parra, J.C.; Benavides, J.M.; Olmos-Severiche, C.A.; Vásquez-Salazar, R.D.; Valdés-Quintero, J.; Mateus, S.; Díaz-Paz, J.P.; Díez, L.; García, A.F.; et al. Assessing the Impacts of Land Cover and Climate Changes on Streamflow Dynamics in the Río Negro Basin (Colombia) Under Present and Future Scenarios. *Hydrology* **2025**, *12*, 281. [CrossRef]
15. Parida, S.; Paul, J.C.; Paramaguru, P.K.; Malik, S. Quantifying soil erosion and identifying sites for conservation measures using geospatial technology in Tilga watershed, Odisha, India. *J. Agric. Eng.* **2025**, *62*, 135–151. [CrossRef]
16. Pimenta, J.; Fernandes, J.N.; Azevedo, A. Remote Sensing Tool for Reservoir Volume Estimation. *Remote Sens.* **2025**, *17*, 619. [CrossRef]
17. Lee, J.; Shin, H. Agricultural Reservoir Operation Strategy Considering Climate and Policy Changes. *Sustainability* **2022**, *14*, 9014. [CrossRef]
18. Lee, J.; Shin, H. Assessment of Future Climate Change Impact on an Agricultural Reservoir in South Korea. *Water* **2021**, *13*, 2125. [CrossRef]
19. Tran, T.N.D.; Nguyen, B.Q.; Grodzka-Łukaszewska, M.; Sinicyn, G.; Lakshmi, V. The role of reservoirs under the impacts of climate change on the Srepok River basin, Central Highlands of Vietnam. *Front. Environ. Sci.* **2023**, *11*, 1304845. [CrossRef]
20. Haider, S.; Masood, M.U.; Rashid, M.; Alshehri, F.; Pande, C.B.; Katipoğlu, O.M.; Costache, R. Simulation of the Potential Impacts of Projected Climate and Land Use Change on Runoff under CMIP6 Scenarios. *Water* **2023**, *15*, 3421. [CrossRef]
21. Espanmanesh, V.; Guilpart, E.; Bourgault, M.A.; Tilmant, A. Adapting reservoir operation to climate change in regions with long-term hydrologic persistence. *Clim. Risk Manag.* **2024**, *45*, 100623. [CrossRef]
22. Zhang, K.; Zhao, Z.; Tian, F. Mitigating the impact of increased drought-flood abrupt alternation events under climate change: The role of reservoirs in the Lancang-Mekong River Basin. *Hydrol. Earth Syst. Sci.* **2026**, *30*, 671–691. [CrossRef]
23. Goyburo, A.; Rau, P.; Lavado-Casimiro, W.; Buytaert, W.; Cuadros-Adriazola, J.; Horna, D. Assessment of Present and Future Water Security under Anthropogenic and Climate Changes Using WEAP Model in the Vilcanota-Urubamba Catchment, Cusco, Perú. *Water* **2023**, *15*, 1439. [CrossRef]
24. Rosas, M.A.; Vanacker, V.; Viveen, W.; Gutierrez, R.R.; Huggel, C. The potential impact of climate variability on siltation of Andean reservoirs. *J. Hydrol.* **2020**, *581*, 124396. [CrossRef]
25. Chavez Flores, I.A.; Mendoza Paz, S.; Villazón Gómez, M.F.; Willems, P.; Gobin, A. Impacts of climate change on the hydropower potential of a multipurpose storage system project in Bolivian Andes. *J. Hydrol. Reg. Stud.* **2025**, *62*, 102903. [CrossRef]
26. El-Mahdy, M.E.S.; El-Abd, W.A.; Al-Metwaly, W.M.; El-Kenawy, E.S.M.; Alharbi, A.H.; Amer, G.M.; Radwan, H.G. Modeling flood dynamics in the Sudd wetlands using Google Earth Engine and AI models optimized with metaheuristics in a changing climate. *J. Water Clim. Change* **2026**, *17*, 637–669. [CrossRef]

27. Chancay, J.E.; Espitia-Sarmiento, E.F. Improving Hourly Precipitation Estimates for Flash Flood Modeling in Data-Scarce Andean-Amazon Basins: An Integrative Framework Based on Machine Learning and Multiple Remotely Sensed Data. *Remote Sens.* **2021**, *13*, 4446. [CrossRef]
28. Ekpetere, K.; Abdelkader, M.; Ishaya, S.; Makwe, E.; Ekpetere, P. Integrating Satellite Imagery and Ground-Based Measurements with a Machine Learning Model for Monitoring Lake Dynamics over a Semi-Arid Region. *Hydrology* **2023**, *10*, 78. [CrossRef]
29. Chen, M.; Huang, Y.; Hu, X.; Xue, M.; Hong, Y.; Novoa, H.M.; Martin, E.; McPherson, R.; Zhu, S.; Peraz, A.V.; et al. Arequipa's Water in the Short Future: A Hydrologic Outlook in an Arid Peruvian Andes Region Utilizing Hyperresolution RCM and CREST-VEC Model Simulations Under SSP5-8.5. *Am. J. Water Resour.* **2025**, *13*, 51–62. [CrossRef]
30. Daneshvar, F.; Frankenberger, J.; Bowling, L.; Cherkauer, K.; Novoa, H.; Delgado, E.B. Effect of hydrologic modification and interbasin water transfers on streamflow metrics affecting aquatic ecology in Arequipa, Peru. *J. Hydrol. Reg. Stud.* **2025**, *60*, 102545. [CrossRef]
31. Wei, X.; García-Chevesich, P.; Alejo, F.; García, V.; Martínez, G.; Daneshvar, F.; Bowling, L.; Gonzáles, E.; Krahenbuhl, R.; McCray, J. Hydrologic Analysis of an Intensively Irrigated Area in Southern Peru Using a Crop-Field Scale Framework. *Water* **2021**, *13*, 318. [CrossRef]
32. Utnicka-Łydek, N. Preliminary hydrological forecast for the Majes-Siguas project and problems associated with water management in the Arequipa region in Southwestern Peru. *Geol. Geophys. Environ.* **2012**, *38*, 547–548.
33. Fonkén, M. An Introduction to the Bofedales of the Peruvian High Andes. *Mires Peat* **2014**, *15*, 5. [CrossRef]
34. Oyague, E. Peatlands of the Central Andes Puna, South America. *Wetl. Sci. Pract.* **2020**, *37*, 255–260. [CrossRef]
35. Chimner, R. Andes, Bofedales, and the Communities of Huascarán National Park, Peru. *Wetl. Sci. Pract.* **2020**, *37*, 246–254. [CrossRef]
36. Valois, R.; Schaffer, N.; Figueroa, R.; Maldonado, A.; Yáñez, E.; Hevia, A.; Carrizo, G.Y.; MacDonell, S. Characterizing the Water Storage Capacity and Hydrological Role of Mountain Peatlands in the Arid Andes of North-Central Chile. *Water* **2020**, *12*, 1071. [CrossRef]
37. Gribbin, T.; Mackay, J.; MacDonald, A.; Hannah, D.; Buytaert, W.; Baiker, J.; Montoya, N.; Perry, B.; Seimon, A.; Rado, M.; et al. Bofedal wetland and glacial melt contributions to dry season streamflow in a high-Andean headwater watershed. *Hydrol. Process.* **2024**, *38*, e15237. [CrossRef]
38. Monge-Salazar, M.; Tovar, C.; Cuadros-Adriazola, J.; Baiker, J.; Montesinos-Tubée, D.; Bonnesoeur, V.; Antiporta, J.; Román-Dañobeytia, F.; Fuentealba, B.; Ochoa-Tocachi, B.; et al. Ecohydrology and ecosystem services of a natural and an artificial bofedal wetland in the central Andes. *Sci. Total Environ.* **2022**, *838*, 155968. [CrossRef] [PubMed]
39. Maldonado-Fonkén, M.; Chuquillanqui, H.; Vildoso, B.; Linares-Palomino, R. Plant communities of high-Andean bofedal wetlands across a trans-Andean transect in southern Peru. *Veg. Classif. Surv.* **2024**, *5*, 203–218. [CrossRef]
40. Wunderlich, W.; Lang, M.; Keating, K.; Perez, W.B.; Oshun, J. The role of peat-forming bofedales in sustaining baseflow in the humid puna. *J. Hydrol. Reg. Stud.* **2023**, *47*, 101394. [CrossRef]
41. Ross, A.; Mendoza, M.M.; Drenkhan, F.; Montoya, N.; Baiker, J.; Mackay, J.; Hannah, D.; Buytaert, W. Seasonal water storage and release dynamics of bofedal wetlands in the Central Andes. *Hydrol. Process.* **2023**, *37*, e14940. [CrossRef]
42. Larico, A.J.M.; Medina, S.Z. Application of WASP model for assessment of water quality for eutrophication control for a reservoir in the Peruvian Andes. *Lakes Reserv.* **2019**, *24*, 37–47. [CrossRef]
43. Uro, V.H.R.; Azevedo, J.; Araújo, M.; Silva, R.; Bedoya, J.; Paredes, B.; Ranilla, C.; Vasconcelos, V.; Campos, A. New Report of Cyanobacteria and Cyanotoxins in El Pañe Reservoir: A Threat for Water Quality in High-Andean Sources from PERU. *Toxins* **2024**, *16*, 378. [CrossRef] [PubMed]
44. Thrasher, B.; Khajehei, S.; Kim, J.B.; Brosnan, I. NASA Earth Exchange Downscaled Climate Projections 30 Arcseconds CMIP6. *Sci. Data* **2024**, *11*, 1346. [CrossRef] [PubMed]
45. Funk, C.; Peterson, P.; Landsfeld, M.; Pedreros, D.; Verdin, J.; Shukla, S.; Husak, G.; Rowland, J.; Harrison, L.; Hoell, A.; et al. The climate hazards infrared precipitation with stations—A new environmental record for monitoring extremes. *Sci. Data* **2015**, *2*, 150066. [CrossRef] [PubMed]
46. Muñoz-Sabater, J.; Dutra, E.; Agustí-Panareda, A.; Albergel, C.; Arduini, G.; Balsamo, G.; Boussetta, S.; Choulga, M.; Harrigan, S.; Hersbach, H.; et al. ERA5-Land: A state-of-the-art global reanalysis dataset for land applications. *Earth Syst. Sci. Data* **2021**, *13*, 4349–4383. [CrossRef]
47. AUTODEMA. Datos Hidrológicos del Embalse El Pañe. Autoridad Autónoma de Majes, Arequipa, Perú, 2020. Available online: https://simhei.pems.pe/SIMHEI2/#/public/chili-1 (accessed on 15 January 2026).
48. Friedl, M.; Sulla-Menashe, D. *MODIS/Terra+Aqua Land Cover Type Yearly L3 Global 500m SIN Grid V061*; NASA Land Processes Distributed Active Archive Center: Sioux Falls, SD, USA, 2022. [CrossRef]
49. Hengl, T.; Mendes de Jesus, J.; Heuvelink, G.B.M.; Ruiperez Gonzalez, M.; Kilibarda, M.; Blagotić, A.; Shangguan, W.; Wright, M.N.; Geng, X.; Bauer-Marschallinger, B.; et al. SoilGrids250m: Global gridded soil information based on machine learning. *PLoS ONE* **2017**, *12*, e0169748. [CrossRef] [PubMed]

50. Fernandez-Palomino, C.A.; Hattermann, F.F.; Krysanova, V.; Vega-Jácome, F.; Menz, C.; Gleixner, S.; Bronstert, A. High-resolution climate projection dataset based on CMIP6 for Peru and Ecuador: BASD-CMIP6-PE. *Sci. Data* **2024**, *11*, 34. [CrossRef] [PubMed]
51. Jain, S.; Jaiswal, R.K.; Lohani, A.K.; Galkate, R. Development of cloud-based rainfall–runoff model using Google Earth Engine. *Curr. Sci.* **2021**, *121*, 1433–1440. [CrossRef]
52. Llactayo, V.; Valdivia, J.; Yarleque, C.; Callañaupa, S.; Villalobos-Puma, E.; Guizado, D.; Alvarado-Lugo, R. Future changes of precipitation types in the Peruvian Andes. *Sci. Rep.* **2024**, *14*, 22634. [CrossRef] [PubMed]
53. Moriasi, D.N.; Arnold, J.G.; Van Liew, M.W.; Bingner, R.L.; Harmel, R.D.; Veith, T.L. Model evaluation guidelines for systematic quantification of accuracy in watershed simulations. *Trans. ASABE* **2007**, *50*, 885–900. [CrossRef]
54. Moriasi, D.N.; Gitau, M.W.; Pai, N.; Daggupati, P. Hydrologic and water quality models: Performance measures and evaluation criteria. *Trans. ASABE* **2015**, *58*, 1763–1785. [CrossRef]
55. Enayati, M.; Bozorg-Haddad, O.; Bazrafshan, J.; Hejabi, S.; Chu, X. Bias correction capabilities of quantile mapping methods for rainfall and temperature variables. *J. Water Clim. Change* **2021**, *12*, 401–419. [CrossRef]
56. Villafuerte, E.M.; Angulo, E.C. Evaluating Statistical Bias Correction Techniques to Enhance Precipitation Projections in the Cachi Basin, Peruvian Andes. *Rev. De Gestão Soc. E Ambient.-RGSA* **2024**, *18*, e09204. [CrossRef]
57. Lehner, F.; Nadeem, I.; Formayer, H. Evaluating skills and issues of quantile-based bias adjustment for climate change scenarios. *Adv. Stat. Climatol. Meteorol. Oceanogr.* **2023**, *9*, 29–44. [CrossRef]
58. Cannon, A.J.; Sobie, S.R.; Murdock, T.Q. Bias Correction of GCM Precipitation by Quantile Mapping: How Well Do Methods Preserve Changes in Quantiles and Extremes? *J. Clim.* **2015**, *28*, 6938–6959. [CrossRef]
59. Mendez, M.; Calvo-Valverde, L.A.; Hidalgo-Madriz, J.A.; Araya-Obando, J.A. Assessing the Effect of Bias Correction Methods on the Development of Intensity–Duration–Frequency Curves Based on Projections from the CORDEX Central America GCM-RCM Multimodel-Ensemble. *Water* **2024**, *16*, 3473. [CrossRef]
60. Dinh, T.L.A.; Aires, F. Revisiting the bias correction of climate models for impact studies. *Clim. Change* **2023**, *176*, 140. [CrossRef]

Disclaimer/Publisher's Note: The statements, opinions and data contained in all publications are solely those of the individual author(s) and contributor(s) and not of MDPI and/or the editor(s). MDPI and/or the editor(s) disclaim responsibility for any injury to people or property resulting from any ideas, methods, instructions or products referred to in the content.